Wide angle conoscopic interference patterns in uniaxial crystals

Francisco E. Veiras,[1,*] María T. Garea,[1] and Liliana I. Perez[1,2]

[1]GLOmAe, Departamento de Física, Facultad de Ingeniería, Universidad de Buenos Aires, Av. Paseo Colón 850, Ciudad Autónoma de Buenos Aires, C1063ACV, Argentina

[2]INTECIN CONICET, Av. Paseo Colón 850, Ciudad Autónoma de Buenos Aires, C1063ACV, Argentina

*Corresponding author: fveiras@fi.uba.ar

Received 25 January 2012; accepted 19 March 2012;
posted 23 March 2012 (Doc. ID 162093); published 18 May 2012

The fringe pattern obtained when a divergent (or convergent) beam goes through a sample of birefringent crystal between two crossed polarizers contains information that is inherent to the crystalline sample under study. The formation of fringe patterns is analyzed from distinct approaches and with different degrees of approximation considering cones of light of large numerical aperture. We obtain analytic explicit formulas of the phase shift on the screen and compare them with the exact numerical solution. The results obtained are valid for arbitrary orientation of the optical axis and are not restricted either to low birefringence or to small angles of incidence. Moreover, they enable the extraction of the main features related to the characterization of uniaxial crystal slabs, such as the optical axis tilt angle and the principal refractive indices. © 2012 Optical Society of America

OCIS codes: 100.2650, 160.1190, 230.5440, 260.1180, 260.1440, 260.3160.

1. Introduction

The characterization of uniaxial crystals has been extensively studied since long ago. However, its current importance in diverse fields of science and technology has reencouraged this challenge. Nowadays, high quality liquid crystal displays, spatial light modulators, and birefringent devices demand better characterization [1–4] and modeling [5,6]. Moreover, current trends in technology and science require wide angle illumination systems. The first step deals with the accurate determination of the directions of the optical axis and the measurement of the principal indices: n_e (extraordinary index) and n_o (ordinary index). Several methods have been proposed to measure these characteristics. The measurement methods are generally divided into two types: reflection and transmission. It has been shown in a previous communication [4] that a conoscopic measurement by transmission provides information about a crystal sample. As a starting point, plane-parallel uniaxial crystal samples are studied. Plane-parallel uniaxial plates are quite simple and have been widely used in many devices (e.g., wave retarders). They also constitute the building blocks of more complex devices (e.g., twisted nematic LCDs) [7]. We consider the particular case where the birefringent element only consists of a plane-parallel plate of uniaxial crystal with arbitrary orientation of the optical axis (i.e., arbitrary optical axis tilt angle). The conoscopic measurements are based on the interference between ordinary waves and extraordinary waves due to a crystal plate sandwiched between crossed polarizers when it is illuminated by a cone of light (convergent or divergent). Experimental fringe patterns corresponding to uniaxial crystals [8,9] show a strong dependence on the direction of the optical axis. Moreover, a large numerical aperture (NA) cone of light gives more information about the sample under study [10]. This deviation from the paraxial situation leads us to analyze the differences between paraxial

1559-128X/12/153081-10$15.00/0

and nonparaxial approximations. First, we explain the experimental setup and the models that allow for the description of its results. Second, we analyze the difference between the distinct approximations, their validity, and how to easily extract information on the sample under study.

2. Experimental Setup

There are diverse ways of obtaining a conoscopic interference pattern. We analyze one of the most simple experimental setups that allows us to obtain a wide angle conoscopic interference pattern. It consists of a source of monochromatic linearly polarized light (HeNe laser $\lambda = 632.8$ nm). Then a diffuser (grounded glass) is placed following the beam axis (x axis) in order to expand the beam divergence and generate a smooth speckle pattern of high NA [11–14]. After that, we place a crystal sample of thickness H sandwiched between a polarizer and an analyzer. Then a fringe pattern is collected on a projecting screen that is placed at a distance x_D from the first interface of the crystal (Fig. 1). However, more complex experimental setups can be arranged. For instance, it is also possible to use high NA lenses to get a converging beam and reduce the size of the screen (recording medium).

The intensity of the light on the screen (plane (y,z)) can be calculated as the resulting interference of waves

$$I = I_o + I_e + 2(I_o I_e)^{\frac{1}{2}} \cos \Delta\phi, \tag{1}$$

where the intensities I_o and I_e correspond to the ordinary and the extraordinary beams, respectively, and $\Delta\phi$ corresponds to the phase shift between the ordinary and the extraordinary waves. We do not consider differences between the intensities of both beams. Moreover, the intensities of ordinary and extraordinary beams are considered uniform on the surface of the screen.

3. Ray Tracing for Conical Beams

As known, ray tracing is widely used in optics, due to the fact that it is a fundamental tool for the design of optical instruments. Moreover, it has been used to analyze the first order geometrical deformations that

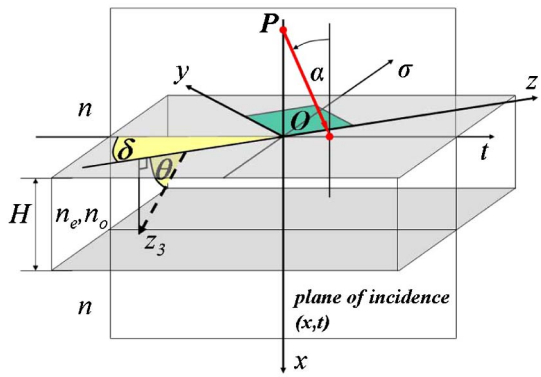

Fig. 2. (Color online) A ray impinging on the first interface ($x = 0$) of a plane-parallel uniaxial plate. (x, σ, t) is the coordinate system associated to the incident wave. x, t is the plane of incidence. As in Fig. 1(b), (x, y, z) is the lab frame. θ is the angle between the optical axis and the interface.

a limited beam suffers when it propagates, reflects, or transmits through an optical device for isotropic or anisotropic media [15–20]. The paraxial or the nonparaxial approaches are used in accordance with the characteristics of the device (material, shape, use, etc.) and the difficulty of ray-tracing formulas. When dealing with anisotropic media, ray tracing for the ordinary wave is the same as in isotropic media, but it is more difficult for the extraordinary wave. In this case, the directions of the normal to the wavefront and the ray direction are generally nonidentical and the ray may not be contained in the plane of incidence. These complex characteristics have stimulated the use of paraxial approximations. Nevertheless, when considering a conic cylindrical beam normally impinging on an arbitrary plane-parallel plate of uniaxial crystal, it is relatively simple to obtain nonparaxial formulas [21–24]. We analyze the transmitted extraordinary rays that correspond to different separate surfaces of impinging rays for distinct apertures. Each ray diverges from (or converges to) point P, which is located along the x axis at $x = x_P$ and impinges on the first interface at an angle of incidence α. The angle δ is the angle between the plane of incidence and the optical axis projection on the interface (Fig. 2). The principal refractive indices of the crystal are n_o and n_e, and the surrounding medium index is n.

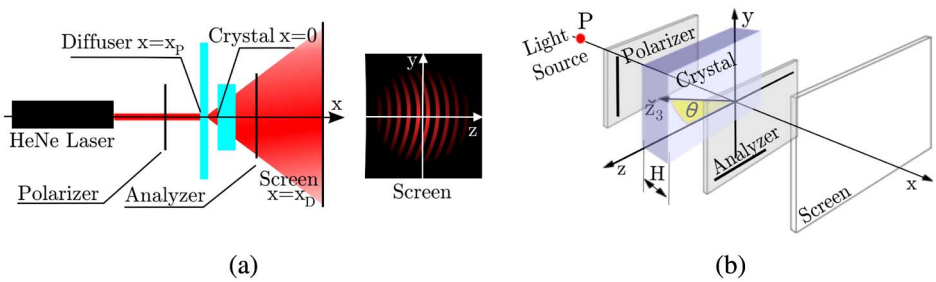

Fig. 1. (Color online) Scheme of the experience. Light propagates in the direction of the x axis, while the screen is placed perpendicular to it. θ is the angle between the optical axis and the interface, (x, y, z), is the lab frame fixed to the first interface of the crystal where z is the projection of the optical axis on the interface of the plate. The diffuser is located at x_P and the screen at x_D.

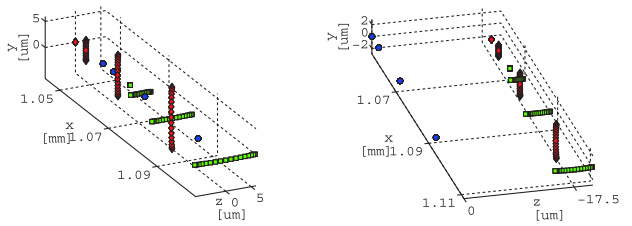

Fig. 3. (Color online) Calculated three-dimensional spot diagram. The blue circles correspond to the points of intersection of ordinary rays (along the x axis). The red diamonds correspond to the extraordinary points $X_{e_Z}(\alpha,\delta)$ (on the plane $z=\Delta_z$), and the green squares correspond to the extraordinary points $X_{e_Y}(\alpha,\delta)$ (on the plane $y=0$) for $\alpha=0°;5°;10°;15°$ and $\delta=0°;10°;\ldots;360°$. $\lambda=632.8$ nm, $n_o=1.5426$, $n_e=1.5516$, $x_P=0$, $H=3$ mm. (a) $\theta=0°$. (b) $\theta=45°$.

By means of exact geometrical ray tracing, it is possible to determine the location of the points of intersection (either real or virtual) of both ordinary and extraordinary rays (Fig. 3). The points of intersection for ordinary rays can be found along the x axis

$$X_o(\alpha)=x_P+H\left[1-\frac{n\cos\alpha}{(n_o^2-n^2\sin^2\alpha)^{\frac{1}{2}}}\right] \tag{2}$$

resulting in a different point on the x axis for each impinging conical surface of rays of aperture α considered. If $x_P<0$, the beam considered is diverging from a point source P, whereas if $x_P>0$, it is converging to a point P. Here x_P is the distance between the first interface and the point P. If $x_P>0$, then P is the point of convergence of a converging beam that is impinging on the plate. On the other hand, if $x_P<0$, then P is the point of divergence of a diverging beam. In both cases, spherically shaped beams impinge on the first interface.

The convergence of extraordinary rays is quite dissimilar. Because of the astigmatism, the points of intersection are located on two principal planes. One of them corresponds to the plane $z=\Delta_z$ [9,25]

$$\Delta_z=-\frac{H(n_e^2-n_o^2)\sin\theta\cos\theta}{n_o^2\cos^2\theta+n_e^2\sin^2\theta}. \tag{3}$$

On this plane, we find the intersection of the pairs of rays corresponding to δ and $(\pi-\delta)$. The x coordinate of the points of intersection on this plane $X_{e_Z}(\alpha,\delta)$ is

$$X_{e_Z}(\alpha,\delta)=x_P+H\left\{1-\frac{nn_e^2n_o\cos\alpha}{h_x[n_e^2h_x-(n_e^2\cos^2\delta+h_x\sin^2\delta)n^2\sin^2\alpha]^{\frac{1}{2}}}\right\}, \tag{4}$$

where $h_x=n_o^2\cos^2\theta+n_e^2\sin^2\theta$ has been defined as an auxiliary parameter in [23]. For the same impinging conical surface of rays, we also find the intersection of the pairs of extraordinary rays corresponding to δ and $-\delta$. In this case, this intersection takes place on the other principal plane corresponding to $y=0$, where the x coordinate $X_{e_Y}(\alpha,\delta)$ of the points of intersection is given by

$$X_{e_Y}(\alpha,\delta)=x_P+H\left\{1-\frac{nn_o\cos\alpha}{[n_e^2h_x-(n_e^2\cos^2\delta+h_x\sin^2\delta)n^2\sin^2\alpha]^{\frac{1}{2}}}\right\}. \tag{5}$$

These exact ray tracing formulas allow us to depict the location of the intersection points of both ordinary and extraordinary rays (Fig. 3). We consider quartz plates ($n_o=1.5426$ and $n_e=1.5516$) in two distinguishable cases of special symmetry. One of them corresponds to the optical axis parallel to the interfaces, i.e., tilt angle $\theta=0$ [Fig. 3(a)]. In this case, the displacement Δ_z is zero [Eq. (3)] and both ordinary and extraordinary beams are coaxial. The other one corresponds to a tilt angle of $\theta=45°$ [Fig. 3(b)]. This value of θ makes the displacement Δ_z approximate to its maximum. The absolute value of this displacement reaches a maximum when the angle between the optical axis and the interfaces is

$$\theta\lfloor_{\Delta_z\max}=\pm\arccos\left[\frac{n_e}{(n_e^2+n_o^2)^{\frac{1}{2}}}\right]. \tag{6}$$

For quartz plane-parallel plates, it corresponds to $\theta=44.83°$. For Fig. 3 we calculated the intersection points that correspond to discrete apertures ($\alpha=0°;5°;10°;15°$). Each impinging conical surface of rays represented by 36 rays (δ in 10° steps) can be analyzed separately. In the ordinary case, each surface of rays results in the intersection of all of its rays in a single point along the x axis. In the extraordinary case, each surface of rays results in the intersection of rays on two lines where each dot along these lines consists in the intersection of two rays (except $\delta=0°;90°;180°;270°$). One of them is parallel to the z axis, and the other is parallel to the y axis. Each extraordinary ray intersects both lines and the screen where the fringe pattern is recovered.

The image of a point object, either real or virtual, in an ideal aberration-free system, is a point where every ray arrives in phase. In the case of aberrated systems, wavefronts are no longer spherical, and consequently rays do not intercept at a single point. For the extraordinary case, it is possible to see that for each value of α, all rays belonging to this conical surface converge into a pair of pseudo-straight lines contained in these principal planes. Degeneration from straight lines, when varying δ, increases as the angle of incidence becomes larger [Figs. 4(a) and 4(b)]. However, this deformation is almost negligible, and it is also possible to see that the distance between these lines and the ordinary points remains almost unchanged for different values of α (Fig. 5). This longitudinal displacement affects both the

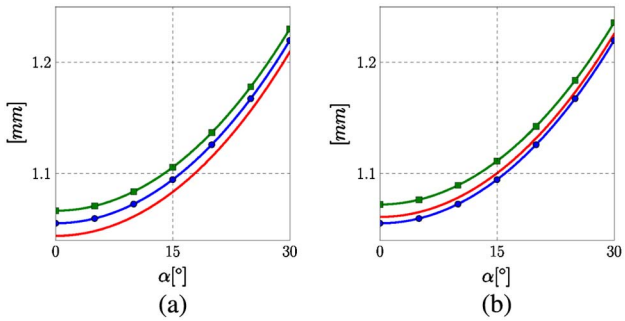

Fig. 4. (Color online) X coordinate of the ordinary and extraordinary intersection points. X_{e_Z} (red solid line). X_{e_Y} (green squares). $X_o(\alpha)$ (blue circles). $0° < \alpha <= 30°$ and $0° < \delta = 360°$; $\lambda = 632.8$ nm, $n_o = 1.5426$, $n_e = 1.5516$, $x_P = 0$, $H = 3$ mm, $D = 10$ cm. (a) $\theta = 0°$. (b) $\theta = 45°$

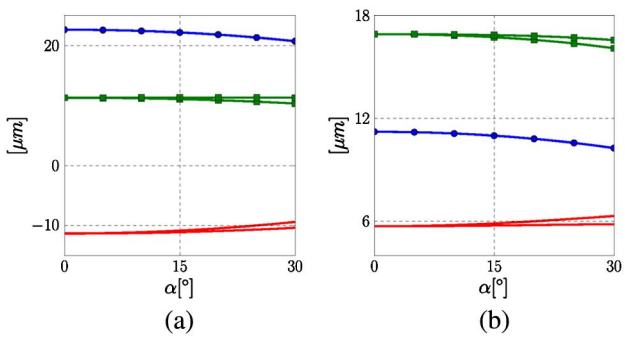

Fig. 5. (Color online) $X_{e_Z} - X_o$ (red solid line), $X_{e_Y} - X_o$ (green squares), and $X_{e_Y} - X_{e_Z}$ (blue circles). $0° < \alpha <= 30°$ and $0° < \delta = 360°$; $\lambda = 632.8$ nm, $n_o = 1.5426$, $n_e = 1.5516$, $x_P = 0$, $H = 3$ mm, $D = 10$ cm. (a) $\theta = 0°$. (b) $\theta = 45°$.

ordinary and the extraordinary wavefronts in a similar way (i.e., we have approximately the same amount of defocus for ordinary and extraordinary waves).

If we take the limit as $\alpha \to 0°$ on Eqs. (2), (4), and (5) (i.e., small angle or paraxial approach), we obtain the location of a point image for the ordinary case and an astigmatic image for the extraordinary case [9]. This way, the ordinary image is located in

$$x_{\text{ord}} = x_P + H\left[1 - \frac{n}{n_o}\right], \tag{7}$$

and the extraordinary image is determined by the localization of the two foci lines

$$x_{e_Z} = x_P + H\left[1 - \frac{n n_e n_o}{(n_o^2 \cos^2\theta + n_e^2 \sin^2\theta)^{\frac{3}{2}}}\right], \tag{8}$$

$$x_{e_Y} = x_P + H\left[1 - \frac{n n_o}{n_e (n_o^2 \cos^2\theta + n_e^2 \sin^2\theta)^{\frac{1}{2}}}\right]. \tag{9}$$

4. Phase Shift Calculation

In this section, we calculate the phase shift by different approaches. We obtain the formulas of the phase shift between waves on the screen of coordinates (x_D, y, z).

A. Image formation approach

This approach is based on previous works [9,25] and relies on the calculation of the position of the geometrical images by paraxial ray tracing. This way, the interference fringes are obtained by superposing the wavefronts emerging from the ordinary image and the extraordinary image. The ordinary image can be found as in isotropic plane-parallel plates [Eq. (7)] resulting in a point image (under paraxial considerations). For the extraordinary image, the three-dimensional distribution of extraordinary rays is such that they all pass through two orthogonal lines. It gives rise to an astigmatic image consisting in two foci lines (Fig. 6). One is parallel to the z axis [Eq. (9)], and the other is perpendicular to it [Eq. (8)]. The ordinary wavefronts are spherically shaped, whereas the extraordinary wavefronts may be written to first order as the superposition of two crossed cylindrical wavefronts.

The phase shift between ordinary and extraordinary waves can be obtained by the resulting interference of these wavefronts. The difference between the spherically shaped ordinary wavefront

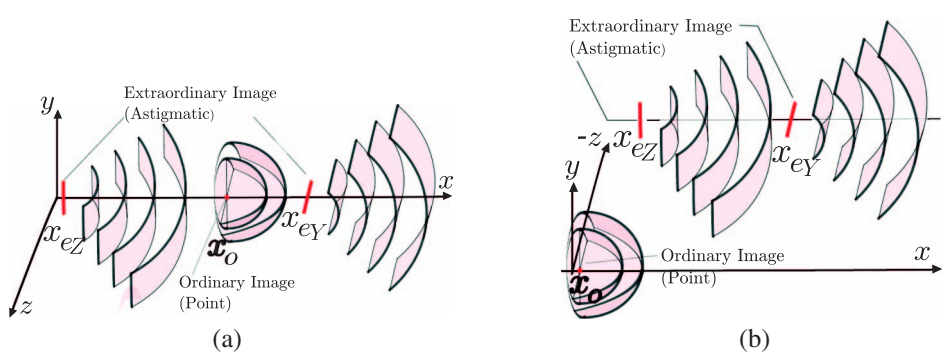

Fig. 6. (Color online) Images and wavefronts. For the ordinary case, there is a point image that originates spherical wavefronts, and for the extraordinary case, there is an astigmatic image that originates cylindrical wavefronts. Once the images are located, it is possible to construct the fringe patterns by superposing the wavefronts that emerge from them. (a) $\theta = 0°$. (b) $\theta = 45°$.

and the astigmatically aberrated extraordinary wavefront gives rise to an optical path difference (OPD) on a plane parallel to the plate of coordinates (x_D, y, z)

$$\Delta\phi_{\text{aberra}} = \frac{2\pi n}{\lambda_v}\left[y^2 \frac{x_o - x_{e_Y}}{2(x_D - x_o)(x_D - x_{e_Y})} + z^2 \frac{x_o - x_{e_Z}}{2(x_D - x_o)(x_D - x_{e_Z})} + z\frac{\Delta_z}{x_D - x_{e_Z}}\right]. \quad (10)$$

Under the assumptions we made, this phase shift takes into account the difference between the aberration-free ordinary wavefront and the aberrated extraordinary wavefront. Higher order aberrations have not been considered in this approach. The aberrations considered are the lateral shift Δ_z and the astigmatism, whereas longitudinal defocus has not been considered, since it has poor influence, as it affects both ordinary and extraordinary wavefronts in a similar way. In order to obtain the total amount of phase shift on the screen, we have to add the OPD between the ordinary and extraordinary waves for normal incidence to $\Delta\phi_{\text{aberra}}(y, z)$,

$$\Delta\phi_{\text{image}}(y, z) = \Delta\phi_{\text{aberra}}(y, z) + \Delta\phi_{\alpha=0}, \quad (11)$$

where $\Delta\phi_{\alpha=0}$ (Eq. (19) in [5]) is the phase difference between the ordinary and extraordinary waves in the center of the screen

$$\Delta\phi_{\alpha=0} = \frac{2\pi}{\lambda_v} H(n_o - n''_{\alpha=0}) \quad (12)$$

with $n''_{\alpha=0}$,

$$n''_{\alpha=0} = \frac{n_o n_e}{(n_o^2 \cos^2\theta + n_e^2 \sin^2\theta)^{\frac{1}{2}}} \quad (13)$$

waves on the screen is given by a conic formula (Eqs. (42)–(44) in [9])

$$\Delta\phi_{\text{image}}(x_D, y, z) \simeq \frac{2\pi H}{\lambda_v}\left(A + n\frac{B}{|\rho|}z + n^2\frac{C_Y}{\rho^2}y^2 + n^2\frac{C_Z}{\rho^2}z^2\right), \quad (14)$$

where for A, B, C_Y, and C_Z,

$$A = n_o - \frac{n_o n_e}{(n_o^2 \cos^2\theta + n_e^2 \sin^2\theta)^{\frac{1}{2}}}, \quad (15)$$

$$B = \frac{(n_o^2 - n_e^2)\sin\theta\cos\theta}{(n_o^2 \cos^2\theta + n_e^2 \sin^2\theta)}, \quad (16)$$

$$C_Y = \frac{n_o^2 - n_e(n_o^2 \cos^2\theta + n_e^2 \sin^2\theta)^{\frac{1}{2}}}{2n_o n_e(n_o^2 \cos^2\theta + n_e^2 \sin^2\theta)^{\frac{1}{2}}}, \quad (17)$$

$$C_Z = \frac{n_o^2 n_e - (n_o^2 \cos^2\theta + n_e^2 \sin^2\theta)^{\frac{3}{2}}}{2n_o(n_o^2 \cos^2\theta + n_e^2 \sin^2\theta)^{\frac{3}{2}}}. \quad (18)$$

On the one hand, the whole expression corresponding to $\Delta\phi_{\text{image}}(x_D, y, z)$ depends on the characteristics of both the uniaxial crystal sample (refractive indices, orientation of the optical axis, and thickness) and the design of the experience (Fig. 1). On the other hand, A, B, C_Y, and C_Z only depend on the principal refractive indices n_o and n_e, and the angle θ between the optical axis and the interfaces.

B. Nonapproximated approach

In a previous communication [5], we obtained an explicit formula for the phase shift introduced by an anisotropic uniaxial plane–parallel plate with arbitrary orientation of the optical axis when the incident plane wave has an arbitrary direction

$$\Delta\phi_{\text{exact}}(\alpha, \delta) = \frac{2\pi H}{\lambda_v}\left((n_o^2 - n^2\sin^2\alpha)^{\frac{1}{2}} + \frac{n(n_o^2 - n_e^2)\sin\theta\cos\theta\cos\delta\sin\alpha}{n_e^2\sin^2\theta + n_o^2\cos^2\theta} + \frac{-n_o\{n_e^2(n_e^2\sin^2\theta + n_o^2\cos^2\theta) - [n_e^2 - (n_e^2 - n_o^2)\cos^2\theta\sin^2\delta]n^2\sin^2\alpha\}^{\frac{1}{2}}}{n_e^2\sin^2\theta + n_o^2\cos^2\theta}\right). \quad (19)$$

being the index of refraction associated to the extraordinary wave for normal incidence.

If the distance between the localization of the paraxial images and the screen is such that $x_D - x_o \simeq x_D - x_{e_Z} \simeq x_D - x_{e_Y}$, we can approximate all of these quantities by $\rho \doteq x_D - x_o$. Thus, by replacing Eqs. (10), (12), and (13) in Eq. (11), we recover the result obtained in [9], where it is shown that the phase shift $\Delta\phi$ between the ordinary and the extraordinary

This expression is also suitable for calculating the phase shift on the screen as long as we place it at the Fraunhofer zone. If the screen is far enough, the distance between the emerging ordinary and extraordinary wavefronts remains almost unchanged, and it is possible to calculate the phase shift by means of Eq. (19). In order to obtain the resulting interference between waves as a function of the coordinates of the screen (x_D, y, z), we have to calculate the phase

shift between them on this surface. Because of its simplicity, we follow the ordinary rays instead of the extraordinary ones that are a bit more difficult. The incident rays impinge with a direction given by (α, δ), and we follow the ordinary ones from the first interface of the plate up to the screen. This way, the coordinates of the screen and the angle of incidence α are exactly related by

$$(y^2 + z^2)^{\frac{1}{2}} = (x_D - H - x_P) \tan \alpha + H \frac{n \sin \alpha}{(n_o^2 - n^2 \sin^2 \alpha)^{\frac{1}{2}}}. \tag{20}$$

It is not possible to obtain an exact explicit analytic expression for α as a function of y, z. However, it is possible to numerically solve Eq. (20) and find for each point of the screen (x_D, y, z) the corresponding value of $\sin \alpha$. For the azimuth angle, δ, it is easy to find the relationship with the screen coordinates

$$\cos \delta = \frac{z}{(y^2 + z^2)^{\frac{1}{2}}}, \sin^2 \delta = \frac{y^2}{y^2 + z^2}. \tag{21}$$

By means of Eqs. (20) and (21), it is possible to numerically obtain the exact phase shift $\Delta\phi_{\text{exact}}(x_D, y, z)$ as a function of the coordinates of the screen and then the corresponding interference pattern. By making approximations, it is possible to obtain explicit expressions of the phase shift as a function of the coordinates of the screen.

1. *Different approximations on the exact phase shift formulas*

The first approximation we proposed is based on a geometry relation between $\sin \alpha$, the points of intersection of the ordinary rays $X_o(\alpha)$ [Eq. (2)], and the coordinates of the screen

$$\sin \alpha = \left\{ \frac{y^2 + z^2}{[x_D - X_o(\alpha)]^2 + y^2 + z^2} \right\}^{\frac{1}{2}}. \tag{22}$$

If $x_D \gg X_o(\alpha)$ for every value of α considered, it is possible to estimate

$$\sin \alpha \simeq \left\{ \frac{y^2 + z^2}{[x_D - x_o]^2 + y^2 + z^2} \right\}^{\frac{1}{2}}. \tag{23}$$

For small angles, we can see that if α tends to zero, $X_o(\alpha)$ tends to x_o. On the other hand, for large values of α (i.e., large values of $y^2 + z^2$), the differences between $x_D - X_o(\alpha)$ and $x_D - x_o$ are minimal in comparison to the value of $y^2 + z^2$. This first approximation allows us to obtain a *quasi nonparaxial* but explicit and analytic expression $\Delta\phi_{\text{QNP}}(x_D, y, z)$ by replacing Eqs. (21) and (23) in Eq. (19). In order to reduce the complexity of $\Delta\phi_{\text{QNP}}(x_D, y, z)$, several approximations could be proposed. Even though higher order expansions could be made, we propose another approximation by developing $\Delta\phi_{\text{exact}}(\alpha, \delta)$ to a second order expansion in $\sin \alpha$

$$\Delta\phi_{\text{sec}}(\alpha, \delta) = \frac{2\pi H}{\lambda_v} [A + B \cos \delta n \sin \alpha + (C_Y \sin^2 \delta + C_Z \cos^2 \delta) n^2 \sin^2 \alpha], \tag{24}$$

where A, B, C_Y, and C_Z coincide with those obtained in Eqs. (15), (16), (17), and (18). If we replace Eqs. (21) and (23) in Eq. (24), we obtain an explicit approximation of the phase shift $\Delta\phi_{\text{sec}}(x_D, y, z)$ (less accurate than $\Delta\phi_{\text{QNP}}(x_D, y, z)$).

Finally, if we expand $\Delta\phi_{\text{QNP}}(x_D, y, z)$ to second order in y, z, we recover the expression corresponding to $\Delta\phi_{\text{image}}(x_D, y, z)$ [Eq. (14)]. Even though it is also possible to develop higher order expansions and find higher order terms, we will thoroughly investigate this expression due to its simplicity.

In the following section, we will compare the different approximations we obtained, $\Delta\phi_{\text{QNP}}(x_D, y, z)$, $\Delta\phi_{\text{sec}}(x_D, y, z)$, and $\Delta\phi_{\text{image}}(x_D, y, z)$, by means of computer generated interferograms. We will analyze the fringe formation by means of these three different explicit formulas of the phase shift, and we will compare them to the exact formulas.

5. Computer Generated Interferograms

The intensity of the light on the screen can be calculated as the resulting interference of waves by replacing the considered value of $\Delta\phi(x_D, y, z)$ in Eq. (1). By means of this formula and the proper parameters, we generate computer intensity images of the fringe patterns that are similar to those that can be experimentally obtained [9]. Since approximations were made around normal incidence, it will be expectable to obtain differences for high NA conoscopic figures. From Eqs. (14), (19), and (24), we can observe that differences between approximations are sensible to large apertures and are also amplified by a factor H/λ_v. In order to make comparisons, we set experimentally achievable practical values of both parameters, which allow us to see the differences due to their corresponding amplification factor: $H = 3$ mm and $\lambda = 632.8$ nm. We placed the point source at $x_P = 0$, just on the first interface of a quartz slab. The screen is placed at $x_D = 10$ cm, and it is a 10 cm × 10 cm square surface.

In order to illustrate the behavior of the crystals, we arbitrarily select three distinct tilt angles of the optical axis, θ (45°; 85°, and $\theta = 5°$), which are examples of the different fringe shapes that uniaxial plane-parallel plates can provide. Figures 7(a), 7(b), and 8(a) were calculated with the exact formulas.

For the case of $\theta = 5°$, fringes are hyperbolas. In Figs. 8(a) and 8(b), we show the results of calculations with the exact formulas and with the less accurate one ($\Delta\phi_{\text{image}}(x_D, y, z)$). Since disparities cannot be fully appreciated, we calculate the subtraction

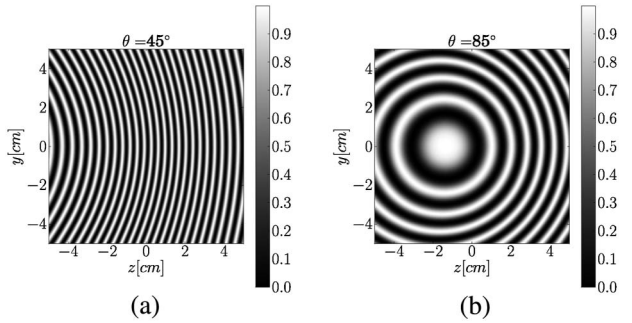

Fig. 7. Interference patterns generated with the exact phase shift formulas. $\lambda = 632.8$ nm, $n_o = 1.5426$, $n_e = 1.5516$, $x_P = 0$, $H = 3$ mm, $x_D = 10$ cm. (a) $\theta = 45°$. (b) $\theta = 85°$.

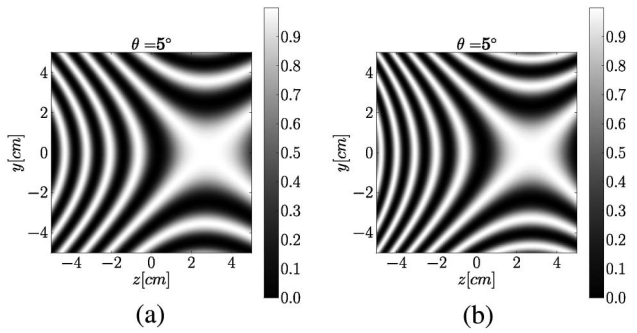

Fig. 8. Interference patterns generated with different phase shift formulas $\Delta\phi(x_D, y, z)$. $\lambda = 632.8$ nm, $n_o = 1.5426$, $n_e = 1.5516$, $\theta = 5°$, $x_P = 0$, $H = 3$ mm, $x_D = 10$ cm. (a) $\Delta\phi_{\text{exact}}(x_D, y, z)$. (b) $\Delta\phi_{\text{image}}(x_D, y, z)$.

between the interference patterns generated (data matrices of the intensity images) with the exact formulas and the ones obtained with different approximations. Figure 9 shows the modulus of the subtraction of the interference pattern generated with $\Delta\phi_{\text{exact}}$ from the patterns generated with the three different approximations of $\Delta\phi$ that correspond to the three approximations proposed. It is possible to appreciate some dissimilarities in the periphery. However, the levels of approximation are notably different according to the graduations of the color bars. We establish the following criterion in order to compare the images obtained with the different approximations:

$$M - N\% = \frac{\sum_{i=1}^{A} \sum_{j=1}^{B} |m_{ij} - n_{ij}|}{AB} 100, \qquad (25)$$

where m_{ij} (n_{ij}) corresponds to the intensity of the pixel located in ith row and jth column of the image M (N), whose pixel size is $A \times B$. This criterion gives an idea of the relative difference between images.

For the case of $\theta = 5°$, we can observe some minimal dissimilitudes due to paraxial approximation in the peripheral region of Fig. 9. The percentage difference obtained with $\Delta\phi_{\text{image}}$ according to the proposed criterion is approximately 22%. This value corresponds to the double summation of the pixels of the whole image from Fig. 9(c) divided by the number of pixels of the image and multiplied by 100 [Eq. (25)]. However, it is possible to note that the hyperbola asymptotes coincide, even for large angles. Instead, if the summation is circumscribed to the center of Fig. 9(c), more precisely to an area of 5 cm × 5 cm, we obtain a percentage difference of approximately 3%. We compare the results obtained with the three different approximations for every tilt angle (θ) of the optical axis. We analyze the results for two cases of different NA, one corresponding to the interference patterns collected by a screen surface of 10 cm × 10 cm (NA $\simeq$ 0.58), and the other one corresponding to the cropped section around the center of 5 cm × 5 cm (NA $\simeq$ 0.33).

In the case of higher NA [Fig. 10(a)], we obtain larger differences due to weakness of the approximations on the periphery of the fringe patterns. However, in the case of the fringe patterns obtained with $\Delta\phi_{\text{QNP}}(x_D, y, z)$, the percentage differences are minimal for both considered NA [Figs. 10(a) and 10(b)]. In the case of lower NA [Fig. 10(b)], the interference pattern obtained with $\Delta\phi_{\text{image}}(x_D, y, z)$ seems to reveal some lack of approximation according to our criterion, particularly for $\theta \simeq 45°$, where there is a maximum discrepancy. It is related to the displacement Δz of the extraordinary beam in the z direction. As this displacement increases, higher order

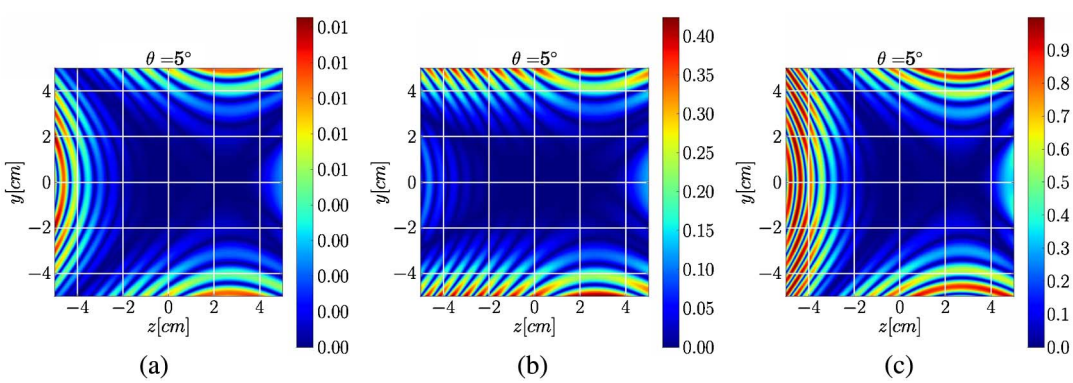

Fig. 9. (Color online) Subtraction (absolute value) of fringe patterns generated with different approximations (*exact-approximated*). $\lambda = 632.8$ nm, $n_o = 1.5426$, $n_e = 1.5516$, $\theta = 5°$, $x_P = 0$, $H = 3$ mm, $x_D = 10$ cm. (a) $\Delta\phi_{\text{QNP}}(x_D, y, z)$, $M - N\% = 0.3\%$. (b) $\Delta\phi_{\text{sec}}(x_D, y, z)$, $M - N\% = 6.43\%$. (c) $\Delta\phi_{\text{image}}(x_D, y, z)$, $M - N\% = 22.4\%$.

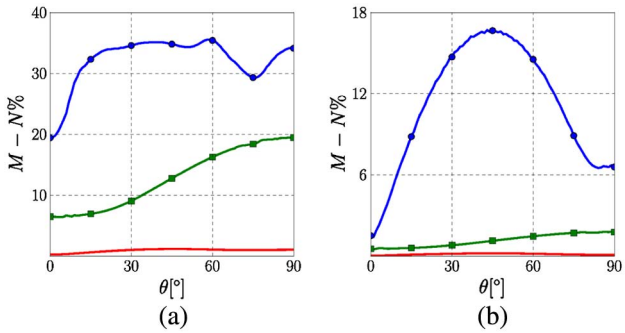

Fig. 10. (Color online) Percentage difference between the interference patterns generated with different phase shift formulas $\Delta\phi(x_D, y, z)$ and the exact formulas. $\Delta\phi_{\mathrm{QNP}}(x_D, y, z)$ (red solid line), $\Delta\phi_{\mathrm{sec}}(x_D, y, z)$ (green squares), and $\Delta\phi_{\mathrm{image}}(x_D, y, z)$ (blue circles). $\lambda = 632.8$ nm, $n_o = 1.5426$, $n_e = 1.5516$, $\theta = 5°$, $x_P = 0$, $H = 3$ mm, $x_D = 10$ cm. (a) 10 cm × 10 cm (NA ≃ 0.58). (b) 5 cm × 5 cm (NA ≃ 0.33).

aberrations (particularly, comma) associated with third order expansions become of significance. For larger NAs, higher order aberrations (even higher than comma) also became of comparable significance, and this maximum is not appreciable.

For both of the apertures considered, the results obtained with $\Delta\phi_{\mathrm{sec}}$ present a similar behavior: the percentage difference increments with θ. $\Delta\phi_{\mathrm{image}}(x_D, y, z)$ is the less accurate formula we propose. Besides its simplicity, it still predicts the behavior of the interference figures, and its applicability will be suitable depending on the NA and the factor of amplification H/λ_v considered.

6. Fringe Shape Analysis

We will analyze the information on a crystal sample that we can get from the shape of the fringes by means of the formula given by Eq. (14). Despite the discrepancies with the more accurate formulas we proposed, this one provides easy-to-read information about the crystal sample. By means of Eq. (14), we can see that equal phase contour lines are conics. The term A [Eq. (15)] is related to the phase shift at normal incidence. It is the phase shift corresponding to the center of the screen, where $y = z = 0$. The dependence on θ is monotonic (monotonically increasing or monotonically decreasing). The absolute value of A [26] reaches its maximum at $\theta = 0°$, i.e., when the optical axis is parallel to the interfaces [Fig. 11(a)]. It is always zero for $\theta = 90°$, i.e., when the optical axis is perpendicular to the interfaces, despite the value of the principal refractive indices. If the incidence is not strictly normal or the optical axis is not perfectly perpendicular to the interfaces, the phase shift introduced will correspond to a zero order OPD; i.e., the OPD will correspond to a fraction of λ_v (commercial devices with such behavior are commonly addressed as *true-zero-order*). The coefficient accompanying the linear term $B/|\rho|$ is associated to the displacement of the extraordinary beam Δ_z [Eq (3)]. This displacement is zero when θ equals 0° or 90° [Figs. 11(b) and 12(b)], and its maximum depends on the principal refractive indices [Eq. (6)]. The coefficients C_Y/ρ^2 and C_Z/ρ^2 [Fig. 11(c)] that accompany the quadratic terms (y^2 and z^2) are those that determine what type of conic we are dealing with [Eqs. (17) and (18)]. When one of them is positive and the other one is negative, we are dealing with hyperbolas. For $C_Z = 0$, we have the particular case of parabolic contours

$$\theta]_{C_Z=0} = \arcsin\left(\left[\frac{(n_o^2 n_e)^{\frac{2}{3}} - n_o^2}{n_e^2 - n_o^2}\right]^{\frac{1}{2}}\right). \tag{26}$$

When both coefficients have the same sign, we obtain ellipses. The case of $\theta = 90°$ is the particular one of $C_Y = C_Z$, and it results in circles.

By looking at the quadratic coefficients, we can recognize two distinct zones where the fringes have different behaviors: hyperbolic and elliptical. It is possible to extract information regarding the crystal by simply calculating the quotient of the coefficients C_Z/C_Y [Fig. 12(a)]. In the hyperbolic region, the slope of the asymptotes is equal to $(-C_Z/C_Y)^{\frac{1}{2}}$, whereas in the elliptical region $(C_Z/C_Y)^{\frac{1}{2}}$ corresponds to the quotient between the axis of the ellipses. It is interesting to note that these quotients

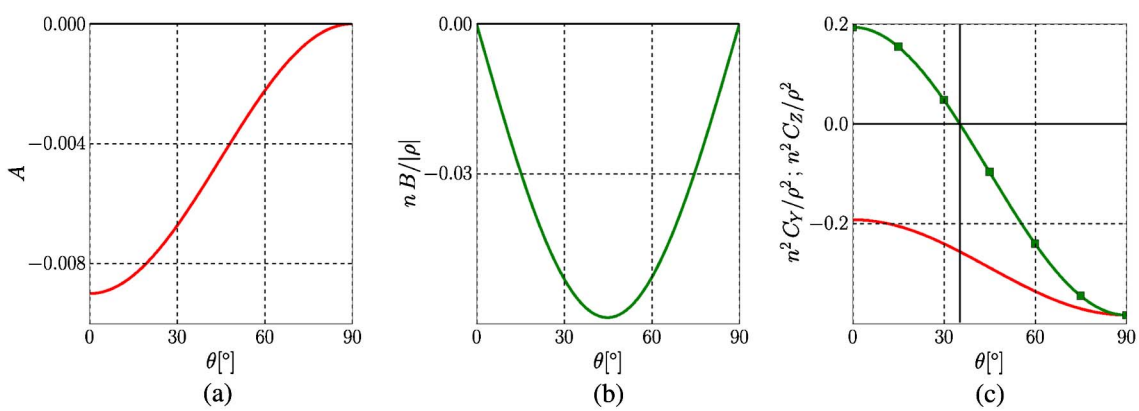

Fig. 11. (Color online) Coefficient analysis. (a) Phase shift for normal incidence A. (b) Linear coefficient $B/|\rho|$. (c) C_Y (red solid line) and C_Z (green squares). $\lambda = 632.8$ nm, $n_o = 1.5426$, $n_e = 1.5516$, $x_P = 0$, $H = 3$ mm, $x_D = 10$ cm.

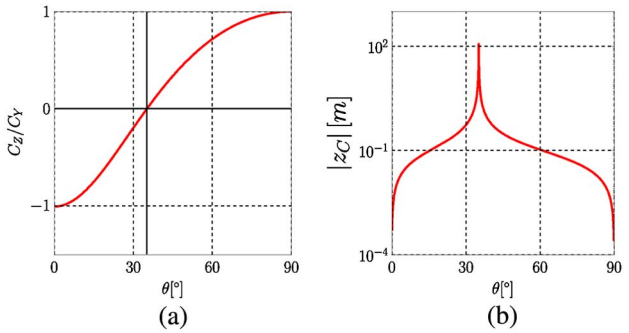

Fig. 12. (Color online) (a) C_Z/C_Y. (b) $|Z_C|$ (logarithmic scale). $\lambda = 632.8$ nm, $n_o = 1.5426$, $n_e = 1.5516$, $x_P = 0$, $x_D = 10$ cm, $H = 3$ mm.

$$\left|\frac{C_Z}{C_Y}\right|^{\frac{1}{2}} = \left|\frac{n_o^2 n_e^2 - n_e h_x^{3/2}}{n_o^2 h_x - n_e h_x^{3/2}}\right|^{1/2} \tag{27}$$

depend only on the principal indices n_o and n_e, and the angle between the optical axis and the interfaces (θ). If $\theta = 90°$, it corresponds to circle shaped fringes, and $|C_Z/C_Y|^{\frac{1}{2}} = 1$. This indicates that both axes of the ellipse are equal. For $\theta = 0$, $|C_Z/C_Y|^{\frac{1}{2}} = (n_e/n_o)^{\frac{1}{2}}$. In the case of quartz for $\lambda = 632.8$ nm, this quotient is approximately 1.003 and corresponds to an angle between the asymptotes and the z axis of 45.08°. For the planes of incidence corresponding to $\delta = \pm 45.08°$, the phase shift will remain unchanged.

It is worth noting that as the optical axis tilt angle θ increases from 0° to 90°, different effects co-occur. On the one hand, the order of phase shift for normal incidence decreases (i.e., the phase difference in number of waves is smaller). On the other hand, the kind of conic changes from hyperbola to circle as the center of the conics moves along the z axis. This latter effect is the reason we do not see the whole ellipses for $\theta = 45°$ [Fig. 7(a)]. The location of the center of the conics z_C is given by $-nB|\rho|/(2n^2 C_Z)$ [Eq. (14)]

$$z_C = \frac{n_o(n_o^2 - n_e^2)h_x \sin\theta \cos\theta\left[x_D - x_P - H\left(1 - \frac{n}{n_o}\right)\right]}{n(n_o^2 n_e - h_x^{\frac{3}{2}})}. \tag{28}$$

When C_Z tends to zero [Eq. (26)], Eq. (28) tends to infinity and the center of the conic is not visible on the screen. As C_Z crosses the zero level, it also changes its sign. In Fig. 12(b), we plot $|z_C|$. For $\theta = 5°$ [Fig. 8(b)], the center of the hyperbola experiences a positive displacement, whereas for $\theta = 85°$ [Fig. 7(b)], the displacement is negative. If the center of the conic is in the region of the screen (i.e., if θ is near 0° or near 90°), it is interesting to note the high sensibility of this parameter regarding the tilt of the optical axis.

7. Conclusions

We developed the formulas of the resulting interference when a converging or diverging beam goes through a uniaxial plane-parallel plate. The methodology we developed relies on exact ray tracing. In this work, we found analytic explicit expressions of the phase shift as a function of the coordinates of the screen. We proposed two approaches for calculating the phase shift: one departs from the paraxial approximation of image formation, and the other one departs from the exact phase shift calculation. In addition to the exact analytical calculation (which requires being numerically solved), we also developed three distinct approximations that demonstrate different accuracies and complexities. Approximations made on the exact formulas show the concordance between the two approaches.

Comparison between the exact solution and the approximated formulas exhibits different performances according to the degree of approximation. The formulas obtained are not limited either to low birefringence or to special cases of optical axis tilt. Moreover, they are applicable for calculating the interference patterns that allow characterization by cones of light of large NA. Depending on the factor H/λ_v, on the NA considered, and on the optical properties of the uniaxial plate, some of the approximated formulas would be more suitable than others. $\Delta\phi_{\mathrm{QNP}}$ presents the best performance and the highest complexity. It is followed by $\Delta\phi_{\mathrm{sec}}$, which makes use of the same approximation on $\sin\alpha$ as $\Delta\phi_{\mathrm{QNP}}$, but has a lower complexity. Finally, $\Delta\phi_{\mathrm{image}}$ allows us to extract information about a uniaxial sample by simple recognition of features from the conoscopic interference patterns. The results obtained will enable us to perform a proper characterization of uniaxial crystals and are useful for a variety of devices that demand wide angle illumination through birefringent crystals.

This work was supported by a grant from Beca Peruilh and two UBACYT grants from Universidad de Buenos Aires (UBACYT 2010–2012 20020090100136 and UBACYT 2011–2014 20020100100139).

References

1. B. Van Horn and H. Winter, "Analysis of the conoscopic measurement for uniaxial liquid-crystal tilt angles," Appl. Opt. **40**, 2089–2094 (2001).
2. D. Su and C. Hsu, "Method for determining the optical axis and (ne, no) of a birefringent crystal," Appl. Opt. **41**, 3936–3940 (2002).
3. P. Lee, J. Pors, M. van Exter, and J. Woerdman, "Simple method for accurate characterization of birefringent crystals," Appl. Opt. **44**, 866–870 (2005).
4. F. E. Veiras, G. Pérez, M. T. Garea, and L. I. Perez, "Characterization of uniaxial crystals through the study of fringe patterns," J. Phys.: Conf. Ser. **274**, 012030 (2011).
5. F. E. Veiras, L. I. Perez, and M. T. Garea, "Phase shift formulas in uniaxial media: an application to waveplates," Appl. Opt. **49**, 2769–2777 (2010).
6. H. Guo, X. Weng, G. Sui, X. Dong, X. Gao, and S. Zhuang, "Propagation of an arbitrary incident light in a uniaxially planar slab," Opt. Commun. **284**, 5509–5512 (2011).

7. D.-K. Yang and S.-T. Wu, *Fundamentals of Liquid Crystal Devices* (Wiley, 2006).
8. M. Françon, *Encyclopedia of Physics. Fundamental of Optics*, S. Flugge, ed.(Springer, 1956), vol. **XXIV**.
9. M. C. Simon and M. T. Garea, "Plane parallel birefringent plates as polarization interferometers," Optik **87**, 95–102 (1991).
10. F. E. Veiras, M. T. Garea, and L. I. Perez, "Fringe pattern analysis by means of wide angle conoscopic illumination of uniaxial crystals," in *Conf. Proc. VII International Conference of young scientists and specialists "Optics–2011"* (St Petersburg, Russia, 17–21 Oct. 2011), pp. 55–57.
11. J. W. Goodman *Speckle Phenomena in Optics: Theory and Applications* (Ben Roberts, 2007).
12. J. W. Goodman, *J W Statistical Optics* (Wiley Classics Library, 2000).
13. A. Gatti, D. Magatti, and F. Ferri, "Three-dimensional coherence of light speckles: theory," Phys. Rev. A **78**, 063806 (2008).
14. D. Magatti, A. Gatti, and F. Ferri, "Three-dimensional coherence of light speckles: experiment," Phys. Rev. A **79**, 053831 (2009).
15. M. A. Alonso, "Exact description of free electromagnetic wave fields in terms of rays," Opt. Express **11**, 3128–3135 (2003).
16. M. Anwar and R. Small, "Geometrical-optics solution for self-focusing in nonlinear optics," J. Opt. Soc. Am. **71**, 124–126 (1981).
17. P. Berczynski, "Complex geometrical optics of nonlinear inhomogeneous fibres," J. Opt. **13**, 035707 (2011).
18. M. Sluijter, M. Xu, H. P. Urbach, and D. K. G. de Boer, "Applicability of geometrical optics to in-plane liquid-crystal configurations," Opt. Lett. **35**, 487–489 (2010).
19. L. I. Perez and M. T. Garea, "Propagation of 2D and 3D Gaussian beams in an anisotropic uniaxial medium: vectorial and scalar treatment," Optik **111**, 297–306 (2000).
20. L. I. Perez, "Nonspecular transverse effects of polarized and unpolarized symmetric beams in isotropic-uniaxial interfaces," J. Opt. Soc. Am. **20**, 741–752 (2003).
21. M. C. Simon, "Ray tracing formulas for monoaxial optical components," Appl. Opt. **22**, 354–360 (1983).
22. M. C. Simon and R. M. Echarri, "Ray tracing formulas for monoaxial optical components: vectorial formulation," Appl. Opt. **25**, 1935–1939 (1986).
23. M. C. Simon and K. V. Gottschalk, "Waves and rays in uniaxial birefringent crystals," Optik **118**, 457–470 (2007).
24. M. C. Simon, L. I. Perez, and F. E. Veiras, "Parallel beams and fans of rays in uniaxial crystals," AIP Conf. Proc. **992**, 714–719 (2008).
25. M. C. Simon, "Image formation through monoaxial plane-parallel plates," Appl. Opt. **27**, 4176–4182 (1988).
26. Note that the sign of A is related to the arbitrary way in which we compute the phase difference between waves: ordinary minus extraordinary.